

# A factor graph EM algorithm for inference of kinetic microstates from patch clamp measurements

Alexander S. Moffett<sup>1</sup>, Guiying Cui<sup>2</sup>, Peter J. Thomas<sup>3</sup>, William D. Hunt<sup>4</sup>, Nael A. McCarty<sup>2</sup>, Ryan S. Westafer<sup>5</sup>, Andrew W. Eckford<sup>1,\*</sup>

**1** Dept. of Electrical Engineering and Computer Science, York University, 4700 Keele Street, Toronto, ON M3J 1P3, Canada

**2** Emory + Children’s Center for Cystic Fibrosis and Airways Disease Research, Emory University School of Medicine and Children’s Healthcare of Atlanta, Atlanta, GA 30322, USA

**3** Dept. of Mathematics, Applied Mathematics, and Statistics, Case Western Reserve University, 10900 Euclid Avenue, Cleveland, OH 44106, USA

**4** School of Electrical and Computer Engineering, Georgia Institute of Technology, 777 Atlantic Drive NW, Atlanta, GA 30332, USA

**5** Georgia Tech Research Institute, 400 10th St NW, Atlanta, GA 30318, USA

\* Corresponding author: aeckford@yorku.ca

## Abstract

We derive a factor graph EM (FGEM) algorithm, a technique that permits combined parameter estimation and statistical inference, to determine hidden kinetic microstates from patch clamp measurements. Using the cystic fibrosis transmembrane conductance regulator (CFTR) and nicotinic acetylcholine receptor (nAChR) as examples, we perform *Monte Carlo* simulations to demonstrate the performance of the algorithm. We show that the performance, measured in terms of the probability of estimation error, approaches the theoretical performance limit of maximum *a posteriori* estimation. Moreover, the algorithm provides a reliability score for its estimates, and we demonstrate that the score can be used to further improve the performance of estimation. We use the algorithm to estimate hidden kinetic states in lab-obtained CFTR single channel patch clamp traces.

## 1 Introduction

The objective of Bayesian inference is to obtain the *a posteriori* probability  $p(x | y)$  of a hidden random variable  $x$  given observations  $y$ . Many algorithms exist for calculating Bayesian inference, either exactly or approximately [1]. In one important class of inference algorithms, the stochastic model is expressed on a graph, and the inference algorithm is performed by

passing messages over this graph. An example of such a graphical representation is the factor graph, where the associated inference algorithm is the sum-product algorithm [2]. Applications of inference algorithms are found in diverse areas such as bioinformatics [3, 4] and biophysics [5, 6], telecommunications, and more recently in machine learning [7].

The classic work of Colquhoun and Hawkes gave an algorithm to estimate transition rates among kinetic microstates, given only observable data such as whether an ion channel was open or closed [8]. Related algorithms have long been known in the signal processing literature, such as the Baum-Welch algorithm [9]; these algorithms are special cases of the Expectation-Maximization (EM) algorithm [10]. Since this early work on inference of kinetic models of ion channels from electrophysiological data, there has been an abundance of work on improving different aspects of analysis using distinct computational approaches. Several methods have been developed to automate idealization of noisy ion channel current recordings, including EM algorithm [11] and deep learning [12] approaches. Non-parametric Bayesian approaches have been used to identify the number of kinetically distinct hidden states without the need to specify a model [13]. Finally, many methods have been developed for estimation of the hidden state transition matrix, including maximum likelihood methods [14, 15, 16, 17, 18] and Bayesian approaches [19, 20, 21, 22].

In this article, we introduce a factor graph EM (FGEM) algorithm [23, 24, 25] which is able to estimate the transition matrix while also yielding maximum likelihood hidden state trajectories from ion channel electrophysiology data. The main advantage of this method is its accuracy and efficiency in calculating *a posteriori* probabilities, meaning the probabilities of hidden states given observations. Our FGEM algorithm thus provides parameter estimates while simultaneously furnishing insight into the hidden ion channel conformational dynamics, given a kinetic model. Although frequently applied to parameter estimation problems in digital signal processing, FGEM algorithms have recently been applied to biomedical signal processing problems [26, 27], and has not hitherto been applied to patch clamp signals.

We apply our inference technique to the cystic fibrosis transmembrane conductance regulator (CFTR) anion channel and a nicotinic acetylcholine receptor (nAChR) [28]. Cystic

fibrosis (CF) is a life-threatening genetic disease affecting the respiratory and digestive systems, caused by mutations to CFTR [29]. CFTR is a “broken” member of the ATP-binding cassette (ABC) transporter class, in that CFTR acts as an ATP-gated ion channel rather than an active transporter as is the function of other ABC transporters. CFTR consists of a single polypeptide chain, with two transmembrane domain (TMD)-nucleotide binding domain (NBD) pairs connected through a region called the R domain [30]. The two TMDs form a gated channel which is controlled by the state of the two intracellular NBDs. Each of the two NBDs contributes to two binding sites for ATP, although only one of these sites facilitates the hydrolysis of ATP to ADP. There are a number of kinetic models of the CFTR cycle, varying in both the number of microstates and the balance between reversible and irreversible transitions [31, 32, 33]. In any model, the steps coupled to ATP hydrolysis must be irreversible, while it can be argued that other transitions may be treated as effectively irreversible [33]. In this work, we use a modified version of the model from Fuller *et al.* [32] (Fig. 1).

nAChRs are ligand-gated ion channels activated by the neurotransmitter acetylcholine (ACh) [34]. nAChRs are composed of five monomers of varying compositions. These subunits are arranged around a central pore, through which ions can flow. There are multiple ACh binding sites, and ACh binding to these sites induces conformational changes in the nAChR which open the channel to  $\text{Na}^+$ ,  $\text{K}^+$ , and  $\text{Ca}^{2+}$  ions [35]. Several kinetic models of the muscular nAChR have been developed [36, 37, 38], accounting for the allosteric nature of ACh-induced nAChR opening [39]. We use a version of the model adapted from [36] (Fig. 2).

We demonstrate the capability of the FGEM algorithm to infer hidden state trajectories with low probability of error for simulated CFTR and nAChR data with varying ligand concentrations and for experimental CFTR current recordings.

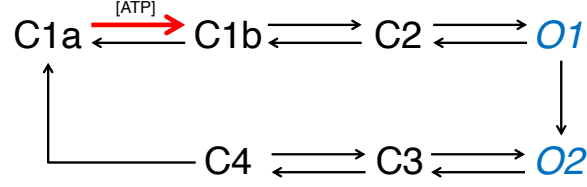


Figure 1: CFTR cycle model. Permitted state transitions are indicated with arrows. State transitions that are sensitive to ATP concentration are indicated with bold red arrows and labelled [ATP]. States with open and closed ion channels are indicated in blue italics and black, respectively. See also reference [32] and equation (2).

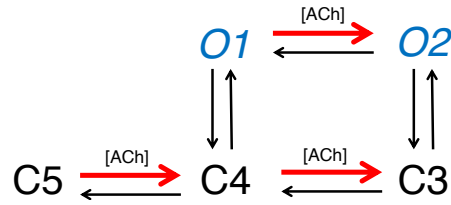


Figure 2: nAChR cycle model. Permitted state transitions are indicated with arrows. State transitions that are sensitive to ACh concentration are indicated with bold red arrows and labelled [ACh]. States with open and closed ion channels are indicated in blue italics and black, respectively. See also references [36, 40] and equation (3).

## 2 Materials and methods

### 2.1 Receptor model

We consider the CFTR and nAChR membrane channels. Both have associated receptor elements—CFTR has receptor regions for ATP and nAChR contains receptors to ACh. These can be modelled using a master equation of the form

$$\frac{dY}{dt} = YR, \quad (1)$$

where  $Y$  is a row vector with length equal to the number of hidden kinetic states, and  $R$  is a square matrix of kinetic rates for each possible state transition. In this formulation,  $Y_i$  is the fraction of receptors in kinetic state  $i$ , while  $R_{ij}$  is the transition rate from state  $i$  to state  $j$ .

In some kinetic states, an ion channel is open, allowing a current to flow; in other states, the channel is closed, allowing no current. A patch clamp measures the current flowing through the channel, indicating whether the membrane channel is open or closed.

For CFTR, we use a purely cyclical model of the ATP-driven CFTR gating cycle, based on the model in [32], as shown in Figure 1. In this 7-state model, states C1a, C1b, and C4 are fully closed, so we assume that ions are completely unable to pass through when CFTR is in these states. States C2 and C3 are closed-permissive states; we assume here that they also pass no current. States O1 and O2 are open states in which chloride can flow through CFTR. Beginning with C1a, with a single ATP bound at the first ATP binding site, the reversible transition to C1b occurs when a second ATP binds so that both binding sites are occupied. Because this step involves ATP binding, the rate depends on the concentration of ATP. The reversible transitions from C1b to C2 and from C2 to O1 are conformational changes resulting in an open CFTR pore. The transition from O1 to O2 is the first of two irreversible steps in the cycle, with one NBD-bound ATP undergoing hydrolysis to ADP. CFTR can then undergo reversible conformational changes from O2 to C3 and from C3 to C4, resulting in a closed pore. Finally, the second irreversible step occurs in the transition from C4 to C1a, where the NBD-bound ADP unbinds from CFTR, leaving one apo and one filled ATP binding site.

The transition rates are given in the rate matrix (with rows and columns, in order, corresponding to C1a, C1b, C2, O1, O2, C3, and C4):

$$R = \begin{bmatrix} R_{11} & k_{C1a \rightarrow C1b} & 0 & 0 & 0 & 0 & 0 \\ k_{C1b \rightarrow C1a} & R_{22} & k_{C1b \rightarrow C2} & 0 & 0 & 0 & 0 \\ 0 & k_{C2 \rightarrow C1b} & R_{33} & k_{C2 \rightarrow O1} & 0 & 0 & 0 \\ 0 & 0 & k_{O1 \rightarrow C2} & R_{44} & k_{O1 \rightarrow O2} & 0 & 0 \\ 0 & 0 & 0 & 0 & R_{55} & k_{O2 \rightarrow C3} & 0 \\ 0 & 0 & 0 & 0 & k_{C3 \rightarrow O2} & R_{66} & k_{C3 \rightarrow C4} \\ k_{C4 \rightarrow C1a} & 0 & 0 & 0 & 0 & k_{C4 \rightarrow C3} & R_{77} \end{bmatrix} \quad (2)$$

with the diagonal entries  $R_{ii}$  set so that each row of  $R$  sums to zero, and with  $R_{ij} = 0$

indicating that the transition  $i \rightarrow j$  is forbidden. For completeness, the full continuous-time master equation describing this system is given in the SI.

Table 1 gives example values for each rate, noting that the value of  $k_{C1a \rightarrow C1b}$  is dependent on the environmental concentration of ATP.

For nAChR, we adapted a 5-state model of the nAChR cycle from [36] (Figure 2). This model includes three closed states (C3, C4, and C5) and two open states (O1 and O2). The transitions from C5 to C4, C4 to C3, and O1 to O2 correspond to binding of acetylcholine to the receptor. These rates are dependent on acetylcholine concentration.

The transition rates are given in the rate matrix (with rows and columns, in order, corresponding to O1, O2, C3, C4, and C5):

$$R = \begin{bmatrix} R_{11} & k_{O1 \rightarrow O2} & 0 & k_{O1 \rightarrow C4} & 0 \\ k_{O2 \rightarrow O1} & R_{22} & k_{O2 \rightarrow C3} & 0 & 0 \\ 0 & k_{C3 \rightarrow O2} & R_{33} & k_{C3 \rightarrow C4} & 0 \\ k_{C4 \rightarrow O1} & 0 & k_{C4 \rightarrow C3} & R_{44} & k_{C4 \rightarrow C5} \\ 0 & 0 & 0 & k_{C5 \rightarrow C4} & R_{55} \end{bmatrix} \quad (3)$$

with the same conditions on  $R$  as in (2). Again, the full master equation is found in the SI.

Values for the rate parameters (taken from [36]) are found in Table 2, noting that  $k_{O1 \rightarrow O2}$ ,  $k_{C5 \rightarrow C4}$ , and  $k_{C4 \rightarrow C3}$  are dependent on ACh concentration.

## 2.2 Inference and patch clamp signals

If all system parameters are known, the sum-product algorithm [2, 41] may be used to determine the *a posteriori* distribution of the kinetic microstates at any time, given the patch clamp observations. Previous approaches to this problem have involved histogram fitting [42].

Formally, in the absence of noise, our system contains a set  $\mathcal{Y}$  of observable states, a set  $\mathcal{S}$  of kinetic microstates, and a mapping  $m : \mathcal{S} \rightarrow \mathcal{Y}$  from microstates to observable states.

Using CFTR as an example, we have

$$\mathcal{Y} = \{0, 1\} \tag{4}$$

$$\mathcal{S} = \{C1a, C1b, C2, C3, C4, O1, O2\} \tag{5}$$

$$m(s) = \begin{cases} 0, & s \in \{C1a, C1b, C2, C3, C4\} \\ 1, & s \in \{O1, O2\} \end{cases} \tag{6}$$

The observable states  $\{0, 1\}$  correspond to the ion channel being closed and open, respectively. The microstates are labelled so that the first letter indicates whether the channel is closed (C) or open (O).

Patch clamp signals are normally sampled in time to form discrete-time signals. Let  $y = [y_1, y_2, \dots, y_n] \in \mathcal{Y}^n$  represent the sequence of observations for a single channel, and let  $s = [s_1, s_2, \dots, s_n] \in \mathcal{S}^n$  represent the corresponding microstates (i.e., for each  $k$ ,  $y_k = m(s_k)$ ). The transitions of microstates  $s_{k-1} \rightarrow s_k$  can be modelled as Markov chains: let  $P = [P_{ij}]$  represent a  $|\mathcal{S}| \times |\mathcal{S}|$  transition probability matrix, with  $P_{ij} = \Pr(s_k = j \mid s_{k-1} = i)$ . (We may also allow  $P$  to be time-varying; in this case we will write the matrix at time  $k$  as  $P^{(k)} = [P_{ij}^{(k)}]$ .)

The stochastic dynamics of the microstates are normally stated in terms of a rate matrix  $R = [R_{ij}]$ , where  $R_{ij}$  is the kinetic rate of the transition from  $i$  to  $j$ . Given  $R$ , and a sufficiently small discrete time step  $\Delta t$ ,  $P$  is given by

$$P = I + R\Delta t + o(\Delta t), \tag{7}$$

where  $I$  is the identity matrix of the same size as  $R$ , and  $\lim_{h \rightarrow 0} (o(h)/h) = 0$ . The master equation is thus converted to a discrete-time Markov chain [43].

Given this system, we use the sum-product algorithm to obtain the *a posteriori* distribution  $p(s_k \mid y)$ , the complete details of which are described in the supplemental information (SI). Given  $p(s_k \mid y)$ , we can then estimate the hidden state by finding the most probable state  $s_k$  given  $y$ , i.e.,

$$\hat{s}_k = \arg \max_{s_k \in \mathcal{S}} p(s_k \mid y), \tag{8}$$

which is known as the maximum *a posteriori* probability (MAP) estimate. It can be shown that the MAP estimate has the lowest probability of error of any estimator.

### 2.3 The factor graph EM algorithm

The transition probability matrix  $P$  (from (7)) is unknown *a priori* and must be estimated from the data. This estimation task must occur alongside the inference of the hidden states. This is a natural setting for the EM algorithm [10].

In our application of the EM algorithm, we treat the nonzero entries of the transition probability matrix  $P$  (and potentially the observation noise variance  $\sigma^2$ ) as unknown parameters. Starting with initial guesses of  $P$  (and  $\sigma^2$ ), the EM algorithm proceeds iteratively. First we perform inference, as though the parameter estimates were equal to their true values (E-step), and then maximize the log of the inferred likelihood function to obtain new estimates of  $P$  (and  $\sigma^2$ ) (M-step). Subsequently these estimates are fed back to the E-step to complete a new iteration.

The factor graph EM algorithm is a variant of the EM algorithm that is intended for use alongside the sum-product algorithm [25, 24]. In particular, the graphical inference performed by the sum-product algorithm is used to calculate the E-step of the algorithm. (Graphical inference can also be used in the M-step, though we do not use this feature.)

A complete derivation of the EM algorithm for our problem is found in the SI.

### 2.4 Simulation

We test the factor graph EM algorithm via Monte Carlo simulation. For our simulations, we discretize time and simulate the receptors using discrete-time Markov chains; this method gives simulated measurements similar to sampled patch clamp traces.

Our figure of merit is *probability of error*: for ground-truth state  $s$  and estimate  $\hat{s}$ , probability of error  $P_e$  is defined as

$$P_e = \Pr(s \neq \hat{s}), \tag{9}$$



i.e., the proportion of microstates that are incorrectly detected.

## 2.5 Patch clamp measurements

Single CFTR channels were studied in inside-out patches pulled from *Xenopus* oocytes injected with cRNA encoding the wildtype channel, as previously described [44]. Briefly, to enable removal of the vitelline membrane, oocytes were placed in a bath solution containing (in mM) 200 monopotassium aspartate, 20 KCl, 1 MgCl<sub>2</sub>, 10 EGTA, and 10 HEPES, pH 7.2 adjusted with KOH. Gigaohm seals were formed with patch pipettes pulled from borosilicate glass and filled with solution containing (in mM) 150 N-methyl-D-glutamine (NMDG) chloride, 5 MgCl<sub>2</sub>, and 10 TES buffer, pH 7.5. After excision of the patch, CFTR channels were activated by bath solution containing 150 mM NMDG chloride, 1.1 mM MgCl<sub>2</sub>, 2 mM Tris-EGTA, 10 mM TES buffer, 1 mM MgATP, and 127 U/ml PKA, pH 7.5. Currents were recorded at  $V_M = -100$  mV using an Axopatch 200B amplifier, with filtering at 0.1-1 kHz.

## 2.6 Code

Code implementing the factor graph EM algorithm, both for generating simulations and analyzing experimental patch clamp data, is available on GitHub, and was used to generate all results in this paper: <http://github.com/andreweckford/PatchClampFactorGraphEM/>

## 3 Results

We first present results using simulated patch clamp measurements. In these results, the true kinetic state can be obtained from the simulator, so the performance of the algorithm can be analyzed in detail. Subsequently, we apply the algorithm to actual patch clamp traces obtained from a CFTR receptor.

### 3.1 Analysis using simulated patch clamp measurements

We apply our state estimation method to two simulated receptors: cystic fibrosis transmembrane conductance regulator (CFTR) and nicotinic acetylcholine (nAChR). Both receptors have multiple hidden kinetic states in both the open and closed configurations. Beyond the brief descriptions below, detailed descriptions of our simulation environment, and our receptor models, are given in the Methods section and in the SI.

We use the seven-state CFTR model from [32] and the five-state nAChR model from [36], which are depicted in Figures 1 and 2, respectively; model parameters are given in Tables 1 and 2, respectively. It is important to note that our algorithm works without knowledge of the parameters, and that these parameters are *only used to generate simulated patch clamp measurements*. A key difference between the models is that kinetic states in CFTR are “hard” to estimate while in nAChR they are “easy” (in a way that will be described in detail in the discussion). However, in both cases we show that the factor graph EM algorithm’s performance is close to the theoretical optimum.

		Destination state						
		C1a	C1b	C2	O1	O2	C3	C4
Origin state	C1a	$9.0 \cdot 10^3 \text{ (M s)}^{-1} \text{ [ATP]}$						
	C1b	$5.0 \text{ s}^{-1}$	$7.7 \text{ s}^{-1}$					
	C2	$5.8 \text{ s}^{-1}$		$4.9 \text{ s}^{-1}$				
	O1	$10.0 \text{ s}^{-1}$			$7.1 \text{ s}^{-1}$			
	O2						$3.0 \text{ s}^{-1}$	
	C3					$7.0 \text{ s}^{-1}$		$6.0 \text{ s}^{-1}$
	C4	$1.7 \text{ s}^{-1}$					$12.8 \text{ s}^{-1}$	

Table 1: Parameters for the CFTR channel, corresponding to the model in Figure 1. A blank entry indicates that the transition is impossible. [ATP] indicates molar concentration of ATP.

In many of these results, we compare a factor graph EM algorithm, which iteratively performs parameter estimation and inference, to factor-graph-based inference, where the

		Destination state				
		O1	O2	C3	C4	C5
Origin state	O1		$5 \cdot 10^8 \text{ (M s)}^{-1} \text{ [ACh]}$		$1 \cdot 10^3 \text{ s}^{-1}$	
	O2	$0.66 \text{ s}^{-1}$		$5 \cdot 10^2 \text{ s}^{-1}$		
	C3		$1.5 \cdot 10^4 \text{ s}^{-1}$		$4 \cdot 10^3 \text{ s}^{-1}$	
	C4	$15 \text{ s}^{-1}$		$5 \cdot 10^8 \text{ (M s)}^{-1} \text{ [ACh]}$		$2 \cdot 10^3 \text{ s}^{-1}$
	C5				$1 \cdot 10^8 \text{ (M s)}^{-1} \text{ [ACh]}$	

Table 2: Parameters for the nAChR receptor, corresponding to the model in Figure 2. A blank entry indicates that the transition is impossible. Parameters are adapted from [36]. [ACh] indicates molar concentration of ACh.

model parameters are known in advance by the algorithm. For factor graphs of the type that we consider, the latter method is known to implement maximum *a posteriori* probability detection, which delivers the minimum probability of error, on average, of any possible algorithm [2].

### 3.1.1 Visualizing the iterative algorithm

The factor graph EM algorithm is iterative, alternating between inference (called the E-step) and estimation of the parameters (called the M-step), with each step updating the other. One full iteration includes both an E-step and an M-step. In Figure 3, we show the progress of the algorithm through 100 iterations, with five simulation runs for each receptor. The probability of error significantly decreases with the number of iterations, although it does not show monotonic behaviour. This may seem surprising since the parameter estimates produced in the M-step are known to be increasing in likelihood with each iteration [10]. However, the probability of error is calculated with respect to inference performed in the E-step, which has no such guarantee.

From the figure it is apparent that the estimates show near-convergence after 100 iterations, though there are still some small changes in  $P_e$ . We chose 100 iterations for easy visualization, and not because the algorithm always converges in this timeframe: we have

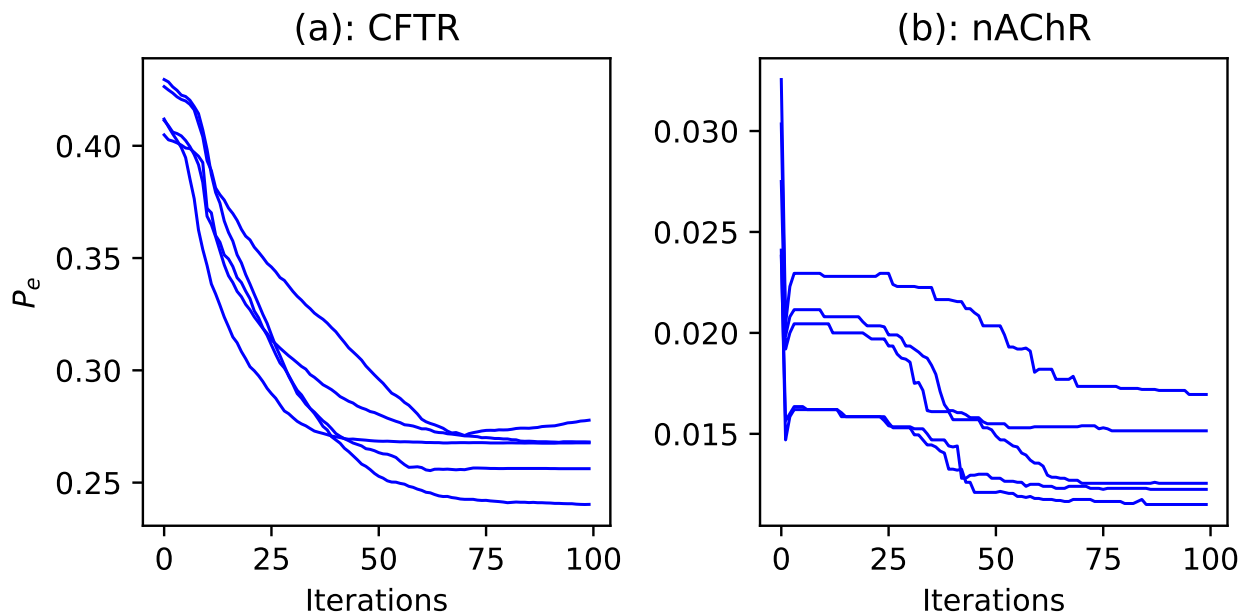


Figure 3: Visualization of the progress of the factor graph EM algorithm, showing the evolution of  $P_e$  as a function of iteration number over five trials in CFTR (subfigure (a)), and nAChR (subfigure (b)). Each plot was generated from simulated patch clamp measurements. CFTR:  $[ATP] = 1.1 \cdot 10^{-3}$  M, sampling rate = 100 Hz; nAChR:  $[ACh] = 1.0 \cdot 10^{-5}$  M, sampling rate = 20 Hz; 20000 samples for each simulation; rate parameters from Tables 1 and 2.

noticed rare cases where the algorithm might still make significant changes after hundreds of iterations, particularly for models with large numbers of parameters like CFTR. For this reason, the rest of our results use larger numbers of iterations.

### 3.1.2 Effect of changing agonist concentration

In both models, most of the model parameters are fixed, but a few are sensitive to the concentration of an agonist (see Tables 1 and 2): CFTR is sensitive to adenosine triphosphate (ATP), while the nAChR receptor is sensitive to the concentration of acetylcholine (ACh). In Figure 4, we show the performance of our algorithm when the concentration of the respective agonist is changed.

We see that there is an effect on the absolute accuracy of estimation as a function of

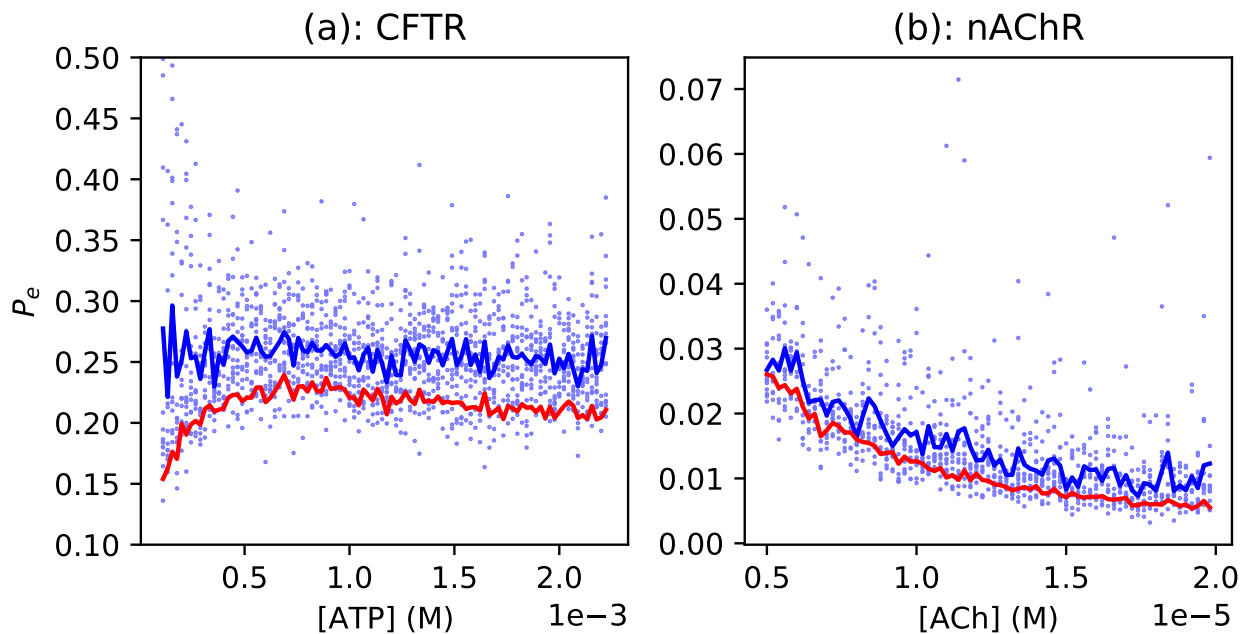


Figure 4: Effect of algorithm performance on changing agonist concentration in CFTR (subfigure (a)) and nAChR (subfigure (b)). *Light blue dots*:  $P_e$  for the factor graph EM algorithm in each simulation. *Blue line*: Average  $P_e$  of the factor graph EM algorithm. *Red line*: Average  $P_e$  of the MAP detector given the true parameter values. CFTR: sampling rate = 100 Hz; nAChR: sampling rate = 20 Hz; 20000 samples and 400 EM iterations for each simulation; rate parameters from Tables 1 and 2. In subfigure (a), two light blue points are cut off at upper left.

concentration. As the concentration of ATP or ACh changes, so does the contribution of distinct microstate transitions to the stationary variance of the recorded current [45], an example of the stochastic shielding phenomenon [46, 47]. For example, at  $[ACh] \sim 20 \mu\text{M}$ , the variance in the observable  $y$  is dominated by noise arising from the  $O2 \rightleftharpoons C3$ , while at  $[ACh] \sim 5 \mu\text{M}$ , the transitions  $O2 \rightleftharpoons C3$ ,  $C3 \rightleftharpoons C4$ , and  $C4 \rightleftharpoons C5$  make roughly equal contributions to the variance (cf. [45], Fig. 2C), which increases the difficulty of unambiguously inferring the microstate given the observed state. Nevertheless, the relative accuracy of the EM algorithm, compared with the estimator given the true parameter values, remains relatively constant.

### 3.1.3 Discarding low-confidence results

The E-step of the factor graph EM algorithm obtains the *a posteriori* probability distribution over the hidden kinetic states, subject to: (1) conditioning on all observed patch clamp measurements, and (2) setting the parameter estimates from the M-step equal to the true parameter values. (This is described in more detail in the Methods section.) The factor graph EM algorithm does not obtain the true *a posteriori* probability, as that would require knowledge of the system parameters. However, this value can be used as a score of the algorithm’s confidence in an estimate, so that estimates with low confidence can be discarded.

In Figure 5, we show the performance of the algorithm when results with confidence score of  $c < 0.8$  are excluded. Note that if  $c$  was the true *a posteriori* probability, then  $c = 0.8$  would correspond to  $P_e = 1 - 0.8 = 0.2$ . Comparing Figure 5 to Figure 4, with CFTR the  $P_e$  is significantly greater than the chosen  $c$ , so if  $c$  is a good approximation for  $P_e$ , relatively few results would have high confidence. Indeed, this behaviour is apparent from the CFTR figure: for estimates with  $c \geq 0.8$ , we have  $P_e \simeq 0.2$  on average, but only a third (or less) of the time series achieves  $c \geq 0.8$ . Meanwhile, with nAChR, there is little improvement in performance since  $P_e$  was already quite low; however, very few estimates are rejected with  $c < 0.8$  (the number of rejected estimates is so low that we do not plot it in this figure).

### 3.1.4 Noisy measurements

In the previous results, the algorithm was provided noiseless knowledge of the state of the ion channel, i.e., the algorithm could tell perfectly if the ion channel was open or closed. While this is a useful assumption for determining the best possible performance of the algorithm, and for illustrating our approach, realistic patch clamp measurements are noisy.

We use an additive Gaussian noise model to represent the patch clamp measurement. That is, the patch clamp observes  $Y$ , where

$$Y = I_{s_k} + N, \tag{10}$$

in which  $I_{s_k}$  (in picoamps) is the current corresponding to kinetic state  $s_k$ , and  $N$  (in picoamps) is additive Gaussian noise with variance  $\sigma^2$ . The EM algorithm then estimates

both the transition probability matrix  $P$  and the noise variance  $\sigma^2$ , a detailed algorithm for which is provided in the SI. Results are shown in Figure 6, in which  $\sigma^2 = 0.1$ . As expected, the noise degrades the accuracy of the estimates, but the EM algorithm still performs well compared with a sum-product algorithm with known parameters.

### 3.2 Application to patch clamp measurements

In Figure 7, we show the application of our algorithm to CFTR patch clamp measurements. We show two examples, corresponding to two different experiments. For techniques used to obtain these measurements, see the Methods section.

Prior to applying the patch clamp signal to the factor graph EM algorithm, we perform a preprocessing step. This step consists of block averaging (i.e., taking the sample average over non-overlapping blocks of 50 samples) and scaling (multiplying by a scalar, here 1.75, so that most signal features are in the range from 0 to 1). This step is performed to reduce noise and improve the performance of the algorithm.

In the bottom plots, we give the patch clamp measurement (light blue line), estimate after 10 EM iterations (grey line), and the estimate after 100 EM iterations (red line). Estimates judged with high confidence (as described above) are highlighted as orange lines. Results from different numbers of iterations are presented to illustrate the progress of the algorithm, while the result from the highest number of iterations would normally be used. From the raw data and preprocessed traces (purple and black lines, respectively), the periods in which the ion channel admits higher current correspond well to the times when the EM algorithm estimates an open state. Moreover, the EM algorithm gives useful estimates of hidden states.

It should be emphasized that the hidden state estimate is the most likely estimate at each time, and might not have the features of a valid trajectory. For example, the EM algorithm rarely decides that CFTR is in state C4; however, the mechanics of the receptor mean that most valid trajectories should pass through C4. This may be because C4 is a briefly-occupied state, and because observations into and out of C4 are not directly observable [40]. Thus the EM algorithm does not have the opportunity to gather evidence that the receptor is

occupying this state.

## 4 Discussion

The model-based factor graph EM algorithm approach is highly flexible and extensible. In terms of receptors, while we presented two examples in this paper (CFTR and nAChR), the approach could in principle be used on any receptor with an ion channel, as long as a kinetic model is available. Notably, machine learning approaches to approximate inference can incorporate the EM algorithm [48]. In terms of techniques, the inference-based approach can be easily extended for use in combination with other instruments or techniques as long as a stochastic model exists for them. Moreover, the factor graph EM algorithm has significant advantages. It is relatively easy to derive and implement, and no training phase is required. Further, as indicated in our results, the performance in terms of  $P_e$  is close to the theoretical optimum.

The algorithm presented in this paper is applied retrospectively to a complete patch clamp trace collected in the laboratory. As such, if particular kinetic microstates are of interest in an experiment, our algorithm can be used to identify when those microstates occur, measuring the effect of any interventions. This feature gives the designer of an experiment a novel and fine-grained algorithmic tool to discover changes to the behaviour of receptor proteins. For example, this method could be used to determine the fine-grained, microstate-by-microstate effects of particular agonists or mutations.

Looking towards future work, reliable estimation of the hidden kinetic state of a receptor could lead to new experimental approaches by targeting those individual states in real time. With adjustments, especially incorporating recursive or “on-line” variants of the EM algorithm [49], our method could be adapted to provide immediate estimates of the hidden state while an experiment is ongoing. An intervention specific to the microstate, for example using targeted electromagnetic radiation [50, 51], could then be used to influence the hidden state, either forcing it to exit or remain in the targeted state. In principle, this method could also be used to design new therapeutic interventions.



## 5 Conclusion

We have demonstrated that the factor graph EM algorithm is an accurate method for estimating the hidden kinetic states from patch clamp current measurements, given an underlying kinetic model with unknown parameters. The methods demonstrated in this paper may be applied widely, to virtually any ion channel. Our work opens up the possibility of novel experimental designs that can exploit fine-grained kinetic state estimation. There is also a rich potential for future theoretical work, such as adapting the algorithm to incorporate other observations alongside the patch clamp, and deriving an algorithm that can handle multiple simultaneous open channels.

## Acknowledgments

ASM and AWE were funded by DARPA via the RadioBio program under grant number HR001117C0125. PJT was supported by NSF via grant number DMS-2052109 and by Oberlin College. WDH, NAM, and RSW were funded in part by DARPA via the RadioBio program under grant number HR001117C0124.

## References

- [1] David MacKay. *Information Theory, Inference and Learning Algorithms*. Cambridge University Press, 2003.
- [2] Frank R Kschischang, Brendan J Frey, and H-A Loeliger. Factor graphs and the sum-product algorithm. *IEEE Transactions on Information Theory*, 47(2):498–519, 2001.
- [3] Hui Yuan Xiong, Yoseph Barash, and Brendan J Frey. Bayesian prediction of tissue-regulated splicing using rna sequence and cellular context. *Bioinformatics*, 27(18):2554–2562, 2011.
- [4] Xavier Meyer, Linda Dib, Daniele Silvestro, and Nicolas Salamin. Simultaneous bayesian inference of phylogeny and molecular coevolution. *Proceedings of the National Academy of Sciences*, 116(11):5027–5036, 2019.
- [5] Philipp Metzner, Frank Noé, and Christof Schütte. Estimating the sampling error: Distribution of transition matrices and functions of transition matrices for given trajectory data. *Physical Review E*, 80(2):021106, 2009.

- [6] Wojciech Potrzebowski, Jill Trehwella, and Ingemar Andre. Bayesian inference of protein conformational ensembles from limited structural data. *PLoS computational biology*, 14(12):e1006641, 2018.
- [7] David Barber. *Bayesian reasoning and machine learning*. Cambridge University Press, 2012.
- [8] David Colquhoun and AG Hawkes. On the stochastic properties of single ion channels. *Proceedings of the Royal Society of London. Series B. Biological Sciences*, 211(1183):205–235, 1981.
- [9] Leonard E Baum, Ted Petrie, George Soules, and Norman Weiss. A maximization technique occurring in the statistical analysis of probabilistic functions of markov chains. *The Annals of Mathematical Statistics*, 41(1):164–171, 1970.
- [10] Arthur P Dempster, Nan M Laird, and Donald B Rubin. Maximum likelihood from incomplete data via the EM algorithm. *Journal of the Royal Statistical Society: Series B (Methodological)*, 39(1):1–22, 1977.
- [11] Syed Islamuddin Shah, Angelo Demuro, Don-On Daniel Mak, Ian Parker, John E Pearson, and Ghanim Ullah. Tracespecks: a software for automated idealization of noisy patch-clamp and imaging data. *Biophysical Journal*, 115(1):9–21, 2018.
- [12] Numan Celik, Fiona O’Brien, Sean Brennan, Richard D Rainbow, Caroline Dart, Yalin Zheng, Frans Coenen, and Richard Barrett-Jolley. Deep-channel uses deep neural networks to detect single-molecule events from patch-clamp data. *Communications Biology*, 3(1):1–10, 2020.
- [13] Keegan E Hines, John R Bankston, and Richard W Aldrich. Analyzing single-molecule time series via nonparametric bayesian inference. *Biophysical Journal*, 108(3):540–556, 2015.
- [14] Feng Qin, Anthony Auerbach, and Frederick Sachs. Estimating single-channel kinetic parameters from idealized patch-clamp data containing missed events. *Biophysical journal*, 70(1):264–280, 1996.
- [15] David Colquhoun, AG Hawkes, and K Srodzinski. Joint distributions of apparent open and shut times of single-ion channels and maximum likelihood fitting of mechanisms. *Philosophical Transactions of the Royal Society of London. Series A: Mathematical, Physical and Engineering Sciences*, 354(1718):2555–2590, 1996.
- [16] D Colquhoun, CJ Hatton, and AG Hawkes. The quality of maximum likelihood estimates of ion channel rate constants. *The Journal of Physiology*, 547(3):699–728, 2003.
- [17] Luciano Moffatt. Estimation of ion channel kinetics from fluctuations of macroscopic currents. *Biophysical journal*, 93(1):74–91, 2007.

- [18] Christopher Nicolai and Frederick Sachs. Solving ion channel kinetics with the qub software. *Biophysical Reviews and Letters*, 8(03n04):191–211, 2013.
- [19] Rafael Rosales, J Alex Stark, William J Fitzgerald, and Stephen B Hladky. Bayesian restoration of ion channel records using hidden markov models. *Biophysical journal*, 80(3):1088–1103, 2001.
- [20] Elan Gin, Martin Falcke, Larry E Wagner, David I Yule, and James Sneyd. Markov chain monte carlo fitting of single-channel data from inositol trisphosphate receptors. *Journal of Theoretical Biology*, 257(3):460–474, 2009.
- [21] Ivo Siekmann, Larry E Wagner II, David Yule, Colin Fox, David Bryant, Edmund J Crampin, and James Sneyd. Mcmc estimation of markov models for ion channels. *Biophysical journal*, 100(8):1919–1929, 2011.
- [22] Michael Epstein, Ben Calderhead, Mark A Girolami, and Lucia G Sivilotti. Bayesian statistical inference in ion-channel models with exact missed event correction. *Biophysical Journal*, 111(2):333–348, 2016.
- [23] Andrew W Eckford. The factor graph EM algorithm: Applications for LDPC codes. In *IEEE 6th Workshop on Signal Processing Advances in Wireless Communications, 2005.*, pages 910–914. IEEE, 2005.
- [24] Hans-Andrea Loeliger, Justin Dauwels, Junli Hu, Sascha Korl, Li Ping, and Frank R Kschischang. The factor graph approach to model-based signal processing. *Proceedings of the IEEE*, 95(6):1295–1322, 2007.
- [25] Justin Dauwels, Andrew Eckford, Sascha Korl, and Hans-Andrea Loeliger. Expectation maximization as message passing-part i: Principles and gaussian messages. *arXiv preprint arXiv:0910.2832*, 2009.
- [26] Federico Wadehn, Thilo Weber, David J Mack, Thomas Heldt, and Hans-Andrea Loeliger. Model-based separation, detection, and classification of eye movements. *IEEE Transactions on Biomedical Engineering*, 67(2):588–600, 2019.
- [27] Federico Wadehn, Thilo Weber, and Hans-Andrea Loeliger. State space models with dynamical and sparse variances, and inference by em message passing. In *2019 27th European Signal Processing Conference (EUSIPCO)*, pages 1–5. IEEE, 2019.
- [28] László Csanády, Paola Vergani, and David C Gadsby. Structure, gating, and regulation of the cftr anion channel. *Physiological Reviews*, 99(1):707–738, 2019.
- [29] Michael M Rey, Michael P Bonk, and Denis Hadjiliadis. Cystic fibrosis: Emerging understanding and therapies. *Annual Review of Medicine*, 70:197–210, 2019.
- [30] Zhe Zhang and Jue Chen. Atomic structure of the cystic fibrosis transmembrane conductance regulator. *Cell*, 167(6):1586–1597, 2016.

- [31] Paola Vergani, Angus C Nairn, and David C Gadsby. On the mechanism of mgatp-dependent gating of cftr  $\text{cl}^-$  channels. *The Journal of General Physiology*, 121(1):17–36, 2003.
- [32] Matthew D Fuller, Zhi-Ren Zhang, Guiying Cui, and Nael A McCarty. The block of cftr by scorpion venom is state-dependent. *Biophysical Journal*, 89(6):3960–3975, 2005.
- [33] László Csanády, Paola Vergani, and David C Gadsby. Strict coupling between cftr’s catalytic cycle and gating of its  $\text{cl}^-$  ion pore revealed by distributions of open channel burst durations. *Proceedings of the National Academy of Sciences*, 107(3):1241–1246, 2010.
- [34] Edson X Albuquerque, Edna FR Pereira, Manickavasagom Alkondon, and Scott W Rogers. Mammalian nicotinic acetylcholine receptors: From structure to function. *Physiological Reviews*, 89(1):73–120, 2009.
- [35] Nigel Unwin. Nicotinic acetylcholine receptor and the structural basis of neuromuscular transmission: insights from torpedo postsynaptic membranes. *Quarterly Reviews of Biophysics*, 46(4):283–322, 2013.
- [36] David Colquhoun and Alan G Hawkes. On the stochastic properties of bursts of single ion channel openings and of clusters of bursts. *Philosophical Transactions of the Royal Society of London. Series B. Biological Sciences*, pages 1–59, 1982.
- [37] Stuart J Edelstein, Olivier Schaad, Eric Henry, Daniel Bertrand, and Jean-Pierre Changeux. A kinetic mechanism for nicotinic acetylcholine receptors based on multiple allosteric transitions. *Biological Cybernetics*, 75(5):361–379, 1996.
- [38] Camila Carignano, Esteban Pablo Barila, and Guillermo Spitzmaul. Analysis of neuronal nicotinic acetylcholine receptor  $\alpha 4\beta 2$  activation at the single-channel level. *Biochimica et Biophysica Acta (BBA)-Biomembranes*, 1858(9):1964–1973, 2016.
- [39] Jean-Pierre Changeux. The nicotinic acetylcholine receptor: a typical ‘allosteric machine’. *Philosophical Transactions of the Royal Society B: Biological Sciences*, 373(1749):20170174, 2018.
- [40] Andrew W Eckford and Peter J Thomas. The channel capacity of channelrhodopsin and other intensity-driven signal transduction receptors. *IEEE Transactions on Molecular, Biological and Multi-Scale Communications*, 4(1):27–38, 2018.
- [41] Andrew W. Eckford. *Low-density parity-check codes for Gilbert-Elliott and Markov-modulated channels*. Ph.D. thesis, University of Toronto, 2004.
- [42] László Csanády. Rapid kinetic analysis of multichannel records by a simultaneous fit to all dwell-time histograms. *Biophysical Journal*, 78(2):785–799, 2000.

- [43] Gregory D Smith. Modeling the stochastic gating of ion channels. In *Computational cell biology*, pages 285–319. Springer, 2002.
- [44] Daniel T Infield, Guiying Cui, Christopher Kuang, and Nael A McCarty. Ion channels and transporters in lung function and disease: Positioning of extracellular loop 1 affects pore gating of the cystic fibrosis transmembrane conductance regulator. *American Journal of Physiology-Lung Cellular and Molecular Physiology*, 310(5):L403, 2016.
- [45] Deena R Schmidt, Roberto F Galán, and Peter J Thomas. Stochastic shielding and edge importance for markov chains with timescale separation. *PLoS computational biology*, 14(6):e1006206, 2018.
- [46] Nicolaus T Schmandt and Roberto F Galán. Stochastic-shielding approximation of markov chains and its application to efficiently simulate random ion-channel gating. *Physical review letters*, 109(11):118101, 2012.
- [47] Deena R Schmidt and Peter J Thomas. Measuring edge importance: A quantitative analysis of the stochastic shielding approximation for random processes on graphs. *The Journal of Mathematical Neuroscience*, 4(1):1–52, 2014.
- [48] Ian Goodfellow, Yoshua Bengio, and Aaron Courville. *Deep learning*. MIT press Cambridge, 2016.
- [49] Olivier Cappé and Eric Moulines. On-line expectation–maximization algorithm for latent data models. *Journal of the Royal Statistical Society: Series B (Statistical Methodology)*, 71(3):593–613, 2009.
- [50] David A Turton, Hans Martin Senn, Thomas Harwood, Adrian J Laphorn, Elizabeth M Ellis, and Klaas Wynne. Terahertz underdamped vibrational motion governs protein-ligand binding in solution. *Nature communications*, 5(1):1–6, 2014.
- [51] Hadeel Elayan, Andrew W. Eckford, and Raviraj S. Adve. Information rates of controlled protein interactions using terahertz communication. *IEEE Transactions on NanoBioscience*, 20(1):9–19, 2021.

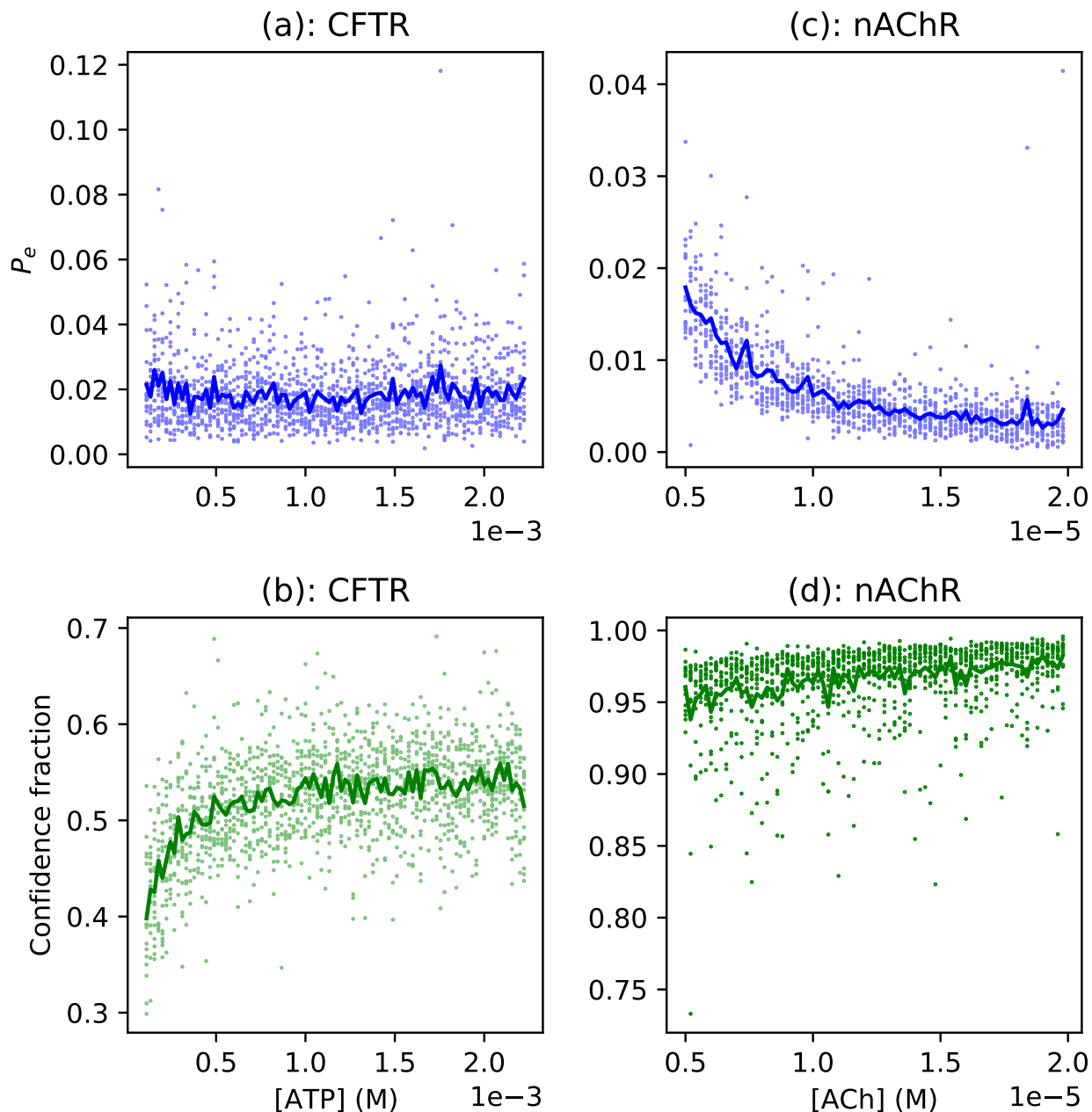


Figure 5: Accuracy of algorithm with low-confidence estimates discarded in CFTR (subfigures (a), (b)) and nAChR (subfigures (c), (d)). In both figures, individually estimated states with a confidence of  $c < 0.8$  are discarded. **Top row (subfigures (a), (c)):** *Light blue dots:*  $P_e$  for all estimates with  $c \geq 0.8$  in each run. *Blue line:* Average  $P_e$  of the algorithm for all estimates with  $c \geq 0.8$ . **Bottom row (subfigures (b), (d)):** *Light green dots:* Fraction of samples with  $c \geq 0.8$  in each run. *Green line:* Average fraction of samples with  $c \geq 0.8$ . CFTR: sampling rate = 100 Hz; nAChR: sampling rate = 20 Hz; 20000 samples and 400 EM iterations for each simulation; rate parameters from Tables 1 and 2.

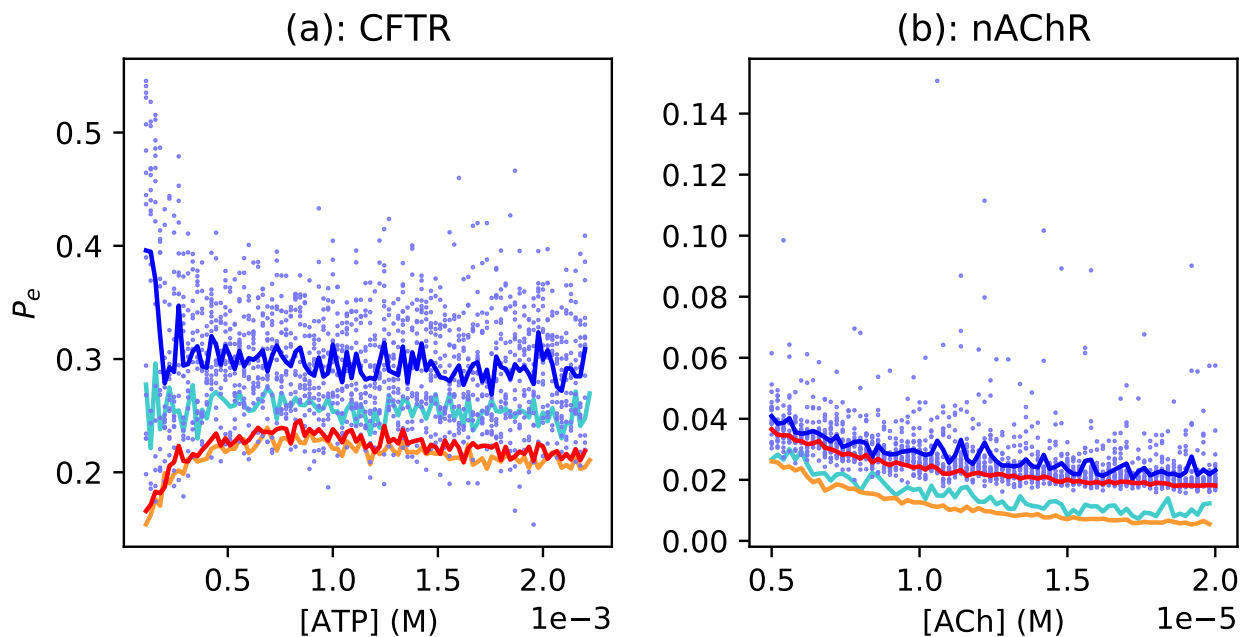


Figure 6: Accuracy of the algorithm for changing input concentration with noisy patch clamp measurements for CFTR (subfigure (a)) and nAChR (subfigure (b)); setup is similar to Figure 4 but Gaussian noise with  $\sigma^2 = 0.1$  is added. *Light blue dots*:  $P_e$  for the factor graph EM algorithm in each simulation. *Blue line*: Average  $P_e$  of the factor graph EM algorithm. *Red line*: Average  $P_e$  of the MAP detector given the true parameter values. *Orange and cyan lines*: Identical to the red and blue lines (respectively) from Figure 4, for comparison. CFTR: sampling rate = 100 Hz; nAChR: sampling rate = 20 Hz; 20000 samples and 400 EM iterations for each simulation; rate parameters from Tables 1 and 2.

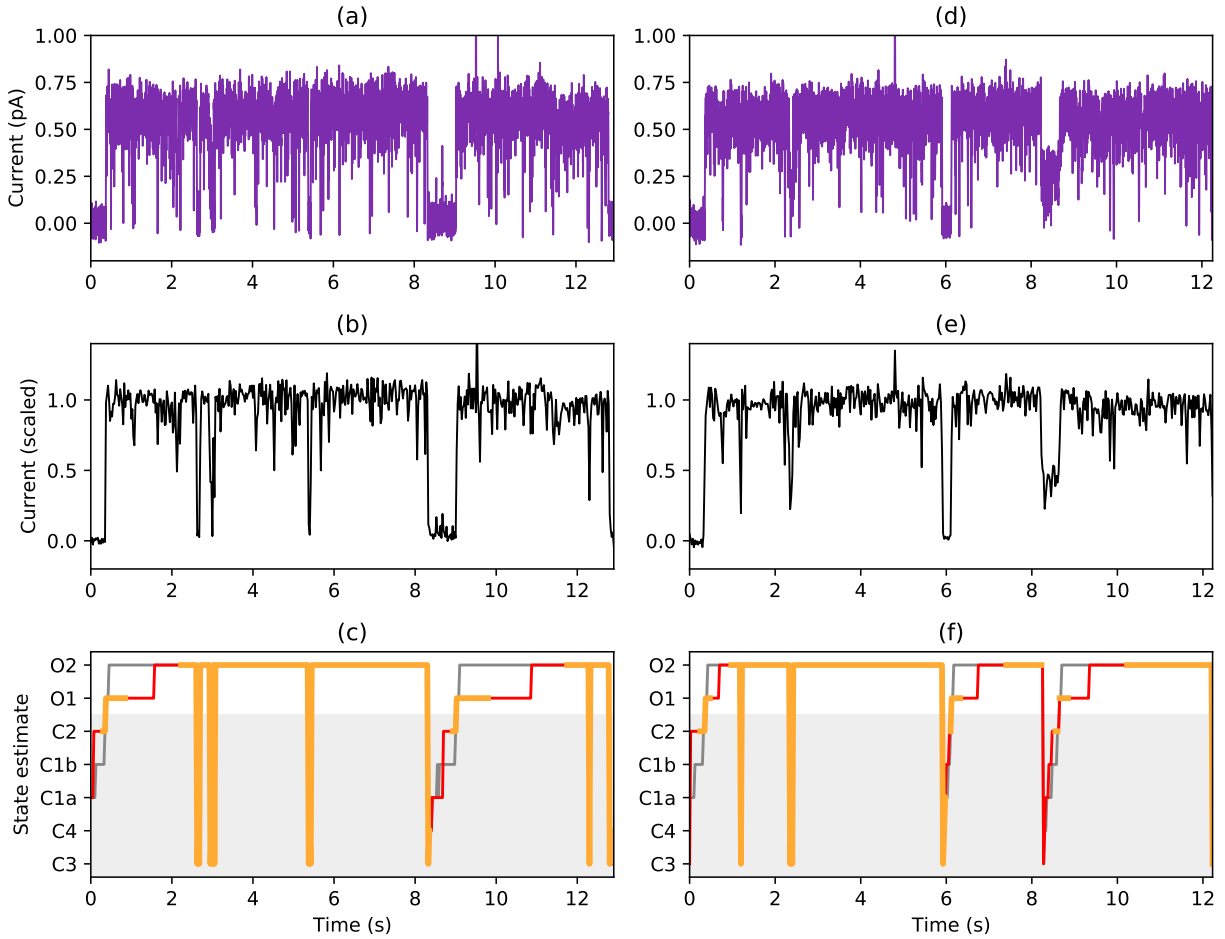


Figure 7: CFTR patch clamp measurements (raw and preprocessed) along with the corresponding hidden state estimates for two different experiments, one in each column. **Top row (subfigures (a), (d)):** *Purple line:* measured patch clamp current. **Middle row (subfigures (b), (e)):** *Black line:* patch clamp current signal after filtering and preprocessing; this signal is provided to the factor graph EM algorithm. **Bottom row (subfigures (c), (f)):** *Grey line:* estimated kinetic state after 10 EM iterations; *orange/red line:* estimated kinetic state after 100 EM iterations, where orange points exceed confidence threshold of 0.8, and red points are below confidence threshold. In the bottom plots, open channel states have a white background, while closed channel states have a light grey background.



# Supplemental Information

## S1 Master equations

### S1.1 CFTR

Consider the master equation from equation (1) in the main paper. Here  $Y$  gives the occupancy probabilities for each microstate. In the case of the CFTR receptor,

$$Y = \left[ P(\text{C1a}), P(\text{C1b}), P(\text{C2}), P(\text{O1}), P(\text{O2}), P(\text{C3}), P(\text{C4}) \right]. \quad (\text{S1})$$

Using (S1) and equation (2) in the main paper, the continuous-time master equation is fully expanded by

$$\frac{dP(\text{C1a})}{dt} = -k_{\text{C1a} \rightarrow \text{C1b}} P(\text{C1a}) + k_{\text{C4} \rightarrow \text{C1a}} P(\text{C4}) + k_{\text{C1b} \rightarrow \text{C1a}} P(\text{C1b}) \quad (\text{S2})$$

$$\frac{dP(\text{C1b})}{dt} = -(k_{\text{C1b} \rightarrow \text{C2}} + k_{\text{C1b} \rightarrow \text{C1a}}) P(\text{C1b}) + k_{\text{C1a} \rightarrow \text{C1b}} P(\text{C1a}) + k_{\text{C2} \rightarrow \text{C1b}} P(\text{C2}) \quad (\text{S3})$$

$$\frac{dP(\text{C2})}{dt} = -(k_{\text{C2} \rightarrow \text{O1}} + k_{\text{C2} \rightarrow \text{C1b}}) P(\text{C2}) + k_{\text{C1b} \rightarrow \text{C2}} P(\text{C1b}) + k_{\text{O1} \rightarrow \text{C2}} P(\text{O1}) \quad (\text{S4})$$

$$\frac{dP(\text{O1})}{dt} = -(k_{\text{O1} \rightarrow \text{O2}} + k_{\text{O1} \rightarrow \text{C2}}) P(\text{O1}) + k_{\text{C2} \rightarrow \text{O1}} P(\text{C2}) \quad (\text{S5})$$

$$\frac{dP(\text{O2})}{dt} = -k_{\text{O2} \rightarrow \text{C3}} P(\text{O2}) + k_{\text{O1} \rightarrow \text{O2}} P(\text{O1}) + k_{\text{C3} \rightarrow \text{O2}} P(\text{C3}) \quad (\text{S6})$$

$$\frac{dP(\text{C3})}{dt} = -(k_{\text{C3} \rightarrow \text{C4}} + k_{\text{C3} \rightarrow \text{O2}}) P(\text{C3}) + k_{\text{O2} \rightarrow \text{C3}} P(\text{O2}) + k_{\text{C4} \rightarrow \text{C3}} P(\text{C4}) \quad (\text{S7})$$

$$\frac{dP(\text{C4})}{dt} = -(k_{\text{C4} \rightarrow \text{C1a}} + k_{\text{C4} \rightarrow \text{C3}}) P(\text{C4}) + k_{\text{C3} \rightarrow \text{C4}} P(\text{C3}). \quad (\text{S8})$$

Example values of each rate are given in Table 1 in the main paper. We suppress the dependence of  $k_{\text{C1a} \rightarrow \text{C1b}}$  on ATP concentration in our notation for the sake of compactness, but as noted in Table 1 the effects of ATP concentration are fully considered in the model.

## S1.2 nAChR

Performing a similar expansion to the above, now  $Y$  gives the occupancy probabilities for nAChR microstates, i.e.,

$$Y = \left[ P(O1), P(O2), P(C3), P(C4), P(C5) \right]. \quad (\text{S9})$$

The continuous-time master equation describing the nAChR cycle is

$$\frac{dP(O1)}{dt} = -(k_{O1 \rightarrow O2} + k_{O1 \rightarrow C4})P(O1) + k_{C4 \rightarrow O1}P(C4) + k_{O2 \rightarrow O1}P(O2) \quad (\text{S10})$$

$$\frac{dP(O2)}{dt} = -(k_{O2 \rightarrow C3} + k_{O2 \rightarrow O1})P(O2) + k_{O1 \rightarrow O2}P(O1) + k_{C3 \rightarrow O2}P(C3) \quad (\text{S11})$$

$$\frac{dP(C3)}{dt} = -(k_{C3 \rightarrow C4} + k_{C3 \rightarrow O2})P(C3) + k_{O2 \rightarrow C3}P(O2) + k_{C4 \rightarrow C3}P(C4) \quad (\text{S12})$$

$$\frac{dP(C4)}{dt} = -(k_{C4 \rightarrow C5} + k_{C4 \rightarrow O1} + k_{C4 \rightarrow C3})P(C4) \quad (\text{S13})$$

$$+ k_{C3 \rightarrow C4}P(C3) + k_{O1 \rightarrow C4}P(O1) + k_{C5 \rightarrow C4}P(C5)$$

$$\frac{dP(C5)}{dt} = -k_{C5 \rightarrow C4}P(C5) + k_{C4 \rightarrow C5}P(C4). \quad (\text{S14})$$

Example rates are described in Table 2 in the main paper. As with the dependence of our CFTR model on ATP concentration, we suppress the dependence of  $k_{O1 \rightarrow O2}$ ,  $k_{C5 \rightarrow C4}$ , and  $k_{C4 \rightarrow C3}$  on acetylcholine concentration in our notation.

## S2 Factor graphs and the sum-product algorithm

### S2.1 General considerations

Factor graphs and the sum-product algorithm are general methods for probabilistic inference, and can in principle be applied to any inference problem using a given stochastic model. Here, for brevity, we focus on the special case of inference in our CFTR model; for more details and generalizations, the reader is encouraged to consult [2].

Consider first the case of a single channel. The probability mass function of  $s$  can be

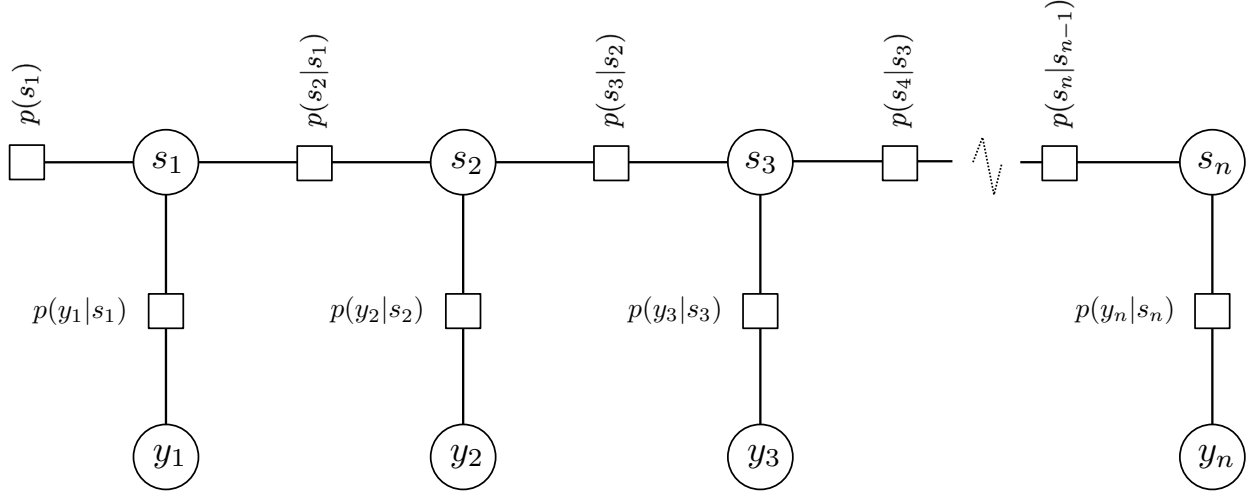


Figure S1: Factor graph for the patch clamp observations.

written

$$p(s) = \prod_{k=1}^n p(s_k | s_{k-1}), \quad (\text{S15})$$

where  $s_0$  is null, i.e.,  $p(s_1 | s_0) = p(s_1)$ . We can include  $y$  in the probabilistic model: since  $y_k$  is deterministic given  $s_k$ , the probability of  $y_k$  given  $s_k$  is the Kronecker delta function between  $y_k$  and  $m(s_k)$ :

$$p(y_k | s_k) = \begin{cases} 1, & y_k = m(s_k) \\ 0, & y_k \neq m(s_k) \end{cases} \quad (\text{S16})$$

Finally, we have the joint probability mass function

$$p(y, s) = \prod_{k=1}^n p(y_k | s_k) p(s_k | s_{k-1}). \quad (\text{S17})$$

The stochastic model  $p(y, s)$  can be represented on a *factor graph*, where nodes representing variables  $s_1, \dots, s_n$  and  $y_1, \dots, y_n$  are connected to nodes representing factors in (S17), and an edge is drawn from variable to factor if the factor is a function of the variable. The factor graph for (S17) is depicted in Figure S1.

We are interested in the *a posteriori* probability  $p(s_k | y)$ , i.e., the distribution over  $s_k$  knowing the observable state for all time. This can be calculated using the *sum-product algorithm*, which is a message-passing algorithm over the factor graph.

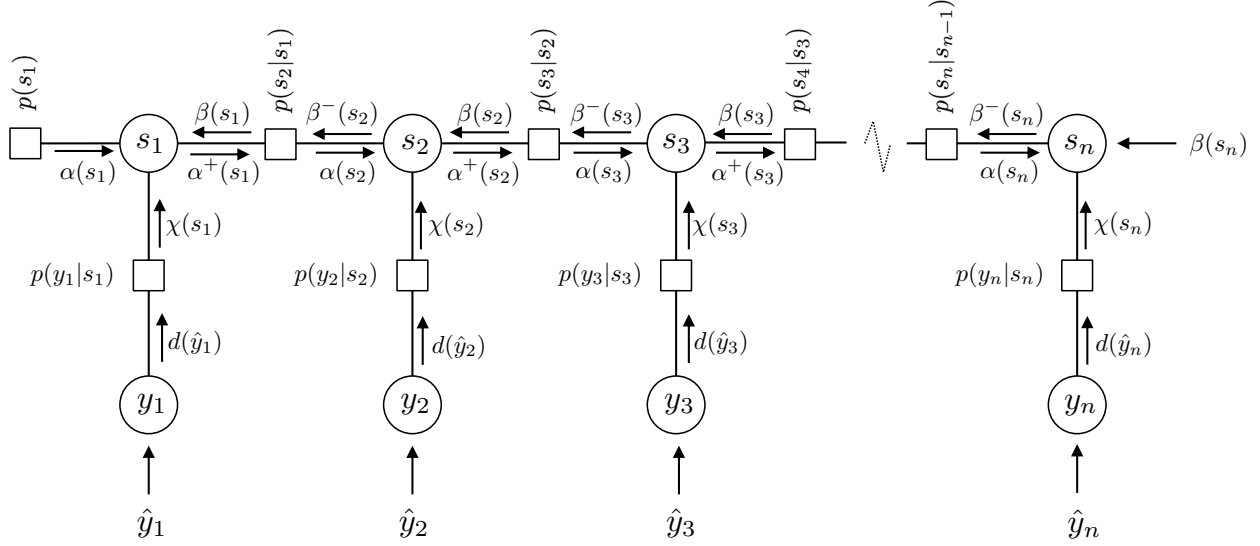


Figure S2: Factor graph for the patch clamp observations with sum-product messages indicated on each edge (cf. Figure S1).

The flow of messages within the factor graph is depicted in Figure S2. *Generally speaking, messages on the outgoing edges from a node are calculated using all incoming messages to that node, **except** the incoming message along the same outgoing edge.*

In terms of the variable nodes  $y_k$ ,  $s_k$ :

- At  $y_k$ , let  $\hat{y}_k$  represent the observed value of  $y_k$ . Then the outgoing message from  $y_k$  is the Kronecker delta function  $\delta(y_k, \hat{y}_k)$ , as the probability is 1 that  $y_k = \hat{y}_k$ . Since  $y_k, \hat{y}_k \in \{0, 1\}$ , this can be represented as a vector  $d(\hat{y}_k) = [\delta(0, \hat{y}_k), \delta(1, \hat{y}_k)]$ , i.e.,:

$$d(\hat{y}_k) = \begin{cases} [1, 0]^T, & \hat{y}_k = 0 \\ [0, 1]^T, & \hat{y}_k = 1 \end{cases} \quad (\text{S18})$$

- At  $s_k$ , the forward message  $\alpha_v^+(s_k)$  is the component-wise product of the incoming forward message  $\alpha_v(s_k)$  and the channel message  $\chi(s_k)$ , defined below; the backward message  $\beta_v^-(s_k)$  is the component-wise product of the incoming backward message  $\beta_v(s_k)$  and the channel message  $\chi(s_k)$ .

It will be convenient to express the forward messages  $\alpha$  as row vectors, and the backward messages  $\beta$  as column vectors.

Representing these message calculations as matrix multiplications,

$$\alpha_v^+(s_k) = \alpha_v(s_k) \text{diag}(\chi(s_k)) \quad (\text{S19})$$

$$\beta_v^-(s_k) = \text{diag}(\chi(s_k)) \beta_v(s_k) \quad (\text{S20})$$

In terms of the factor nodes  $p(y_k | s_k)$ ,  $p(s_k | s_{k-1})$ , each factor node “contains” the factor, and this factor is incorporated into the message calculation. As the factors are conditional probability functions in two variables, it will be convenient to represent the factors as matrices, with the conditional variable remaining constant along the rows, and the probabilistic variable remaining constant along the columns; this implies the matrices are row-stochastic. Message calculations are performed as follows:

- At  $p(y_k | s_k)$ , the factor can be represented by a  $|\mathcal{S}| \times |\mathcal{Y}|$  matrix  $M(s_k, y_k)$ :

$$M(y_k, s_k) = \left[ M_{ij}(s_k, y_k) \right] \quad (\text{S21})$$

where

$$M_{ij}(s_k, y_k) = \Pr(y_k = j | s_k = i) \quad (\text{S22})$$

with slight abuse of the notation:  $y_k = j$  means  $y_k$  is the  $j$ th element of  $\mathcal{Y}$  from (4), and  $s_k = i$  means  $x_k$  is the  $i$ th element of  $\mathcal{S}$  from (5). The channel message  $\chi(s_k)$  is given by the matrix product

$$\chi(s_k) = M(s_k, y_k) d(\hat{y}_k). \quad (\text{S23})$$

- At  $p(s_k | s_{k-1})$ , we have an outgoing forward message  $\alpha(s_k)$  and an outgoing backward message  $\beta(s_{k-1})$ , with an incoming forward message  $\alpha^+(s_{k-1})$  and incoming backward message  $\beta^-(s_k)$ . The internal factor  $p(s_k | s_{k-1})$  is represented by the transition probability matrix  $P$ . The message calculation is given by

$$\alpha(s_k) = \alpha^+(s_{k-1}) P \quad (\text{S24})$$

$$\beta(s_{k-1}) = P \beta^-(s_k) \quad (\text{S25})$$

Combining (S19) and (S24), and (S20) and (S25), we can write

$$\alpha(s_k) = \alpha(s_{k-1}) \text{diag}(\chi(s_{k-1})) P \quad (\text{S26})$$

$$\beta(s_k) = P \text{diag}(\chi(s_{k+1})) \beta(s_{k+1}) \quad (\text{S27})$$

Next we must specify the order in which operations occur, i.e., the message-passing schedule:

- The channel messages  $\chi(s_k)$  are precalculated.
- For the forward messages, the initial forward message  $\alpha(s_1)$  is the steady-state distribution associated with  $P$ . We then iteratively calculate (S26) for each  $k = 2, 3, \dots$
- For the backward messages, we set the initial backward message  $\beta(s_n) = [1, 1, \dots, 1]$  (this message is uninformative, as the future gives us no information). We then iteratively calculate (S27) for each  $k = n - 1, n - 2, \dots$

Finally, to calculate the *a posteriori* probability  $p(s_k | y)$ , we perform the complete message-passing schedule described above. Following the message calculations, we take the product of all messages inbound to variable node  $s_k$ , and normalize (to force the product to sum to 1). Letting  $\odot$  represent componentwise multiplication:

$$p(s_k | y) = \frac{\alpha(s_k) \odot \beta(s_k) \odot \chi(s_k)}{\sum_{s_k} \alpha(s_k) \odot \beta(s_k) \odot \chi(s_k)}. \quad (\text{S28})$$

(Normalizations can also be performed at any intermediate stage of the message calculations, and this is often done for numerical stability.)

### S3 Factor Graph EM algorithm

The message-passing algorithm given in Section S2 requires knowledge of the system parameters, especially the state transition probability matrix  $P$ . (If the patch clamp observations are corrupted by noise, we must also estimate the noise variance  $\sigma^2$ .) As discussed in the main paper, the factor graph EM algorithm incorporates sum-product message passing in each iteration. The algorithm used for our main results is derived below.

### S3.1 Noise-free patch clamp observations

With observations  $y$ , hidden states  $s$ , matrix  $P$  of parameters (i.e. the state transition probability matrix), and estimate  $\bar{P}$  of the parameters, we have

$$Q(P; \bar{P}) = E_{\bar{P}} \left[ \log p(y, s; P) \mid y \right] \quad (\text{S29})$$

where the subscript  $\bar{P}$  indicates that the expectation is taken while setting  $P = \bar{P}$ . From (S17) we can write

$$\begin{aligned} & E_{\bar{P}} \left[ \log p(y, s; P) \mid y \right] \\ &= E_{\bar{P}} \left[ \log \prod_{k=1}^n p(y_k \mid s_k) p(s_k \mid s_{k-1}; P) \mid y \right] \end{aligned} \quad (\text{S30})$$

$$= \sum_{k=1}^n E_{\bar{P}} \left[ \log p(y_k \mid s_k) \mid y \right] + \sum_{k=1}^n E_{\bar{P}} \left[ \log p(s_k \mid s_{k-1}; P) \mid y \right]. \quad (\text{S31})$$

The first term in (S31) is constant with respect to  $P$  and is not important for the rest of the derivation, so we will absorb it into a constant  $C$ . Now we have

$$\begin{aligned} & E_{\bar{P}} \left[ \log p(y, s; P) \mid y \right] \\ &= \sum_{k=1}^n E_{\bar{P}} \left[ \log p(s_k \mid s_{k-1}; P) \mid y \right] + C \end{aligned} \quad (\text{S32})$$

$$= \sum_{k=1}^n \sum_{s_k, s_{k-1}} p(s_k, s_{k-1} \mid y; \bar{P}) \log p(s_k \mid s_{k-1}; P) + C. \quad (\text{S33})$$

The term  $p(s_k, s_{k-1} \mid y; \bar{P})$  can be obtained directly from the sum-product algorithm, as the (normalized) product of all messages incident to the factor node  $p(s_k \mid s_{k-1})$ , setting  $P = \bar{P}$  throughout the factor graph. That is, forming a  $|\mathcal{S}| \times |\mathcal{S}|$  matrix  $Q^{(k)} = [Q_{ij}^{(k)}]$ , where

$$Q^{(k)} = \text{diag}(\alpha^+(s_{k-1})) \bar{P} \text{diag}(\beta^-(s_k)), \quad (\text{S34})$$

we have that  $Q_{ij}^{(k)} = p(s_k = j, s_{k-1} = i \mid y; \bar{P})$ , i.e., we can read the values of  $p(s_k, s_{k-1} \mid y; \bar{P})$  from  $Q^{(k)}$ . Finally, returning to (S33),

$$\begin{aligned} & E_{\bar{P}} \left[ \log p(y, s; P) \mid y \right] \\ &= \sum_{k=1}^n \sum_{s_k, s_{k-1}=(j,i)} Q_{ij}^{(k)} \log P_{ij} + C. \end{aligned} \quad (\text{S35})$$

Calculation of (S35) constitutes the E-step of the EM algorithm.

The M-step is performed as follows. Recall that  $P$  is row-stochastic, so for constant  $i$ ,  $P_{ij}$  forms a probability mass function in  $j$ . With some manipulation (S35) can be rewritten

$$\begin{aligned} & E_{\bar{P}} \left[ \log p(y, s; P) \mid y \right] \\ &= \sum_{s_{k-1}} \sum_{s_k} \sum_{k=1}^n Q_{ij}^{(k)} \log P_{ij} + C \end{aligned} \quad (\text{S36})$$

$$= \sum_{s_{k-1}} Z_i \sum_{s_k} \frac{Q_{ij}}{Z_i} \log P_{ij}, \quad (\text{S37})$$

where

$$Q_{ij} = \sum_{k=1}^n Q_{ij}^{(k)} \quad (\text{S38})$$

$$Z_i = \sum_{s_k} Q_{ij} \quad (\text{S39})$$

Each inner sum of the form  $\sum_{s_k} \frac{Q_{ij}}{Z_i} \log P_{ij}$  is maximized by setting

$$P_{ij} = \frac{Q_{ij}}{Z_i}. \quad (\text{S40})$$

Thus, the M-step is accomplished by forming the matrix  $P = [P_{ij}]$ , with  $P_{ij}$  given by (S40).

### S3.2 Patch clamp observations in Gaussian noise with unknown variance

For the results in Figure 6 in the main paper, we assume that the patch clamp observations could be modelled as

$$Y = I + N, \quad (\text{S41})$$

where  $I$  is the patch clamp current, and  $N$  is an additive white Gaussian noise with zero mean and variance  $\sigma^2$ . Further we assume that  $\sigma^2$  is unknown to the algorithm, and must be estimated in addition to  $P$ .



Here we derive the EM algorithm that jointly estimates  $P$  and  $\sigma^2$ . Modifying (S31), we can write

$$\begin{aligned} & E_{\bar{P}, \bar{\sigma}^2} \left[ \log p(y, s; P, \sigma^2) \right] \\ &= \sum_{k=1}^n E_{\bar{P}, \bar{\sigma}^2} \left[ \log p(y_k | s_k; \sigma^2) | y \right] + \sum_{k=1}^n E_{\bar{P}, \bar{\sigma}^2} \left[ \log p(s_k | s_{k-1}; P) | y \right]. \end{aligned} \quad (\text{S42})$$

In (S42), note that only the first term is a function of  $\sigma^2$ , and only the second term is a function of  $P$ . Thus, the M-step with respect to each parameter can be performed independently. (For  $P$  the M-step is described in detail in the previous section.)

Estimation of  $\sigma^2$  for additive Gaussian noise models such as (S41) is a frequently-used application of the EM algorithm, but we give the derivation here for completeness. Starting with the first term in (S42), we can write

$$\sum_{k=1}^n E_{\bar{P}, \bar{\sigma}^2} \left[ \log p(y_k | s_k; \sigma^2) | y \right] = \sum_{k=1}^n \sum_{s_k} p(s_k | y; \bar{P}, \bar{\sigma}^2) \log p(y_k | s_k; \sigma^2) \quad (\text{S43})$$

The term  $p(s_k | y; \bar{P}, \bar{\sigma}^2)$  is obtained from the sum-product algorithm, and is the *a posteriori* probability of  $s_k$  given  $y$ , obtained from (S28). Meanwhile, letting  $I_{s_k}$  represent the current flowing through the patch clamp in each state  $s_k$ , from (S41) we have

$$\log p(y_k | s_k; \sigma^2) = -\frac{1}{2} \log 2\pi\sigma^2 - \frac{(y_k - I_{s_k})^2}{2\sigma^2}. \quad (\text{S44})$$

Let

$$W = \frac{1}{n} \sum_{k=1}^n \sum_{s_k} (y_k - I_{s_k})^2 p(s_k | y; \bar{P}, \bar{\sigma}^2). \quad (\text{S45})$$

Then (S43) becomes

$$\sum_{k=1}^n E_{\bar{P}, \bar{\sigma}^2} \left[ \log p(y_k | s_k; \sigma^2) | y \right] = -n \frac{1}{2} \log 2\pi\sigma^2 - n \frac{W}{2\sigma^2}. \quad (\text{S46})$$

Calculation of (S46) and (S35) constitute the E-step of this EM algorithm.

In the M-step, it can be shown that the maximizing value of  $\sigma^2$  in (S46) is

$$\sigma^2 = W. \quad (\text{S47})$$

Setting  $\sigma^2$  as in (S47) and  $P_{ij}$  as in (S40) completes the M-step of this EM algorithm.